Dark Matter Results from 54-Ton-Day Exposure of PandaX-II Experiment

Xiangyi Cui,[1] Abdusalam Abdukerim,[2] Wei Chen,[1] Xun Chen,[1] Yunhua Chen,[3] Binbin Dong,[1] Deqing Fang,[4] Changbo Fu,[1] Karl Giboni,[1] Franco Giuliani,[1] Linhui Gu,[1] Yikun Gu,[1] Xuyuan Guo,[3] Zhifan Guo,[5] Ke Han,[1] Changda He,[1] Di Huang,[1] Shengming He,[3] Xingtao Huang,[6] Zhou Huang,[1] Xiangdong Ji,[7,1,§] Yonglin Ju,[5] Shaoli Li,[1] Yao Li,[1] Heng Lin,[1] Huaxuan Liu,[5] Jianglai Liu,[4,7,*] Yugang Ma,[4] Yajun Mao,[8] Kaixiang Ni,[1] Jinhua Ning,[3] Xiangxiang Ren,[1] Fang Shi,[1] Andi Tan,[9,†] Cheng Wang,[5] Hongwei Wang,[4] Meng Wang,[6] Qiuhong Wang,[4,‡] Siguang Wang,[8] Xiuli Wang,[5] Xuming Wang,[1] Qinyu Wu,[1] Shiyong Wu,[3] Mengjiao Xiao,[9,10] Pengwei Xie,[1] Binbin Yan,[6] Yong Yang,[1] Jianfeng Yue,[3] Dan Zhang,[1] Hongguang Zhang,[1] Tao Zhang,[1] Tianqi Zhang,[1] Li Zhao,[1] Jifang Zhou,[3] Ning Zhou,[1] and Xiaopeng Zhou[8]

(PandaX-II Collaboration)

[1]*INPAC and School of Physics and Astronomy, Shanghai Jiao Tong University, Shanghai Laboratory for Particle Physics and Cosmology, Shanghai 200240, China*
[2]*School of Physics and Technology, Xinjiang University, Ürümqi 830046, China*
[3]*Yalong River Hydropower Development Company, Ltd., 288 Shuanglin Road, Chengdu 610051, China*
[4]*Shanghai Institute of Applied Physics, Chinese Academy of Sciences, Shanghai 201800, China*
[5]*School of Mechanical Engineering, Shanghai Jiao Tong University, Shanghai 200240, China*
[6]*School of Physics and Key Laboratory of Particle Physics and Particle Irradiation (MOE), Shandong University, Jinan 250100, China*
[7]*Tsung-Dao Lee Institute, Shanghai 200240, China*
[8]*School of Physics, Peking University, Beijing 100871, China*
[9]*Department of Physics, University of Maryland, College Park, Maryland 20742, USA*
[10]*Center of High Energy Physics, Peking University, Beijing 100871, China*

(Received 24 August 2017; published 30 October 2017)

We report a new search for weakly interacting massive particles (WIMPs) using the combined low background data sets acquired in 2016 and 2017 from the PandaX-II experiment in China. The latest data set contains a new exposure of 77.1 live days, with the background reduced to a level of 0.8×10^{-3} evt/kg/day, improved by a factor of 2.5 in comparison to the previous run in 2016. No excess events are found above the expected background. With a total exposure of 5.4×10^4 kg day, the most stringent upper limit on the spin-independent WIMP-nucleon cross section is set for a WIMP with mass larger than 100 GeV/c^2, with the lowest 90% C.L. exclusion at 8.6×10^{-47} cm^2 at 40 GeV/c^2.

DOI: 10.1103/PhysRevLett.119.181302

Weakly interacting massive particles (WIMPs) are a leading class of dark matter (DM) candidates [1] that have been actively searched for in direct detection experiments using sensitive detectors deployed in the deep underground laboratories around the world. Liquid xenon detectors, such as those constructed and operated by the LUX, PandaX, and XENON collaborations, have been leading in detection capability for heavy-mass WIMPs with masses larger than 10 GeV/c^2 all the way up to a 100 TeV/c^2 or so scale [2–4], which is way beyond the reach of the current generation of colliders. Their detection sensitivities have reached the region predicted by popular theory models (cf. Ref. [5]), which also leave open a 3 order of magnitude discovery space for these exciting experiments [6].

Located in the China Jinping Underground Laboratory (CJPL) [7], the second phase of the PandaX project, PandaX-II, has been under operation since early 2016. PandaX-II is a 580 kg dual-phase xenon time-projection chamber (TPC), with a 60×60 cm cylindrical target viewed by 55 top and 55 bottom Hamamatsu R11410-20 3-in. photomultiplier tubes (PMTs), collecting both the prompt scintillation photons ($S1$) in the liquid and the delayed proportional scintillation photons ($S2$) in the gas. The first low-background physics run (Run 9) collected DM search data for 79.6 live days in 2016, and a world-leading result was published in Ref. [3], in combination with the data obtained during the commissioning period [8]. In this Letter, we report an updated WIMP search using Run 9 and a new 77.1 live day data set taken in 2017 (Run 10) with a significantly lower background level. This Letter presents one of the most sensitive WIMP searches using the largest direct detection exposure to date.

Prior to Run 10, we made an extended calibration for the electron-recoil (ER) events using CH_3T, a technique pioneered by the LUX Collaboration [9]. After the tritium injection, although the getter was initially effective in removing tritium, tritium decay rate eventually plateaued at a rate of 2.0 ± 0.4 μBq/kg, which strongly indicated

tritium attachment on detector surfaces and their slow emanation. In order to eliminate the tritium and to further reduce the krypton background, the detector was emptied and reconditioned, and a redistillation of xenon was carried out on site. In February 2017, the detector was refilled, and the Run 10 dark matter search data set was collected from April to July.

In Run 10, a number of detector PMTs ran at a lower gain than previously, beyond which discharge signals would show up, and as a positive consequence the average dark rate per PMT was reduced from 1.9 to 0.17 kHz. To calibrate the gains of the PMTs, very low intensity blue light emitting diode (LED) runs were taken with the digitizers in full-recording mode (no baseline suppression) twice a week. During the regular data taking, a value of 20 ADC counts relative to the baseline, corresponding to an amplitude of about 0.4 of a single photoelectron (SPE) in Run 9, and 0.6 of a SPE (due to lower gain) in Run 10, was set as the threshold below which the "zero-length encoding" (ZLE) firmware of the CAEN V1724 digitizers suppressed the data recording [10]. The inefficiency to SPE detection due to ZLE was studied channel by channel using the LED calibration runs by comparing the detected photoelectron area with and without the ZLE. The overall efficiency summing over all PMTs for a detected $S1$-like signal of three photoelectrons (PEs) (lower selection window for DM), was 91% and 78%, respectively, during Run 9 and Run 10, indicating that lower gain led to lower ZLE efficiency (see Fig. 6 in the Supplemental Material [11]). This is one significant source of inefficiency that must be taken into account in signal and background modeling.

Out of 110 3-in. PMTs, one top and two bottom ones were kept off in Run 10 (only one bottom PMT was inactive in Run 9). In addition, another peripheral top PMT was noisy; hence, a high ZLE threshold was set under the cost of its low efficiency for small pulses. The cathode high voltage was also lowered to −24 kV (−29 kV in Run 9) to avoid spurious discharges. The gate high voltage was maintained at −4.95 kV, the same as in Run 9. The maximum drift time for an electron changed from 350 μs in Run 9 to 360 μs in Run 10. A field-programmable gate array-based trigger system was implemented to replace the analog trigger, which reduced the trigger threshold for $S2$ to about 50 PE [13]. The electron lifetime in Run 10 was improved to an average of 850 μs, compared with 623 μs in Run 9.

Similar to Ref. [3], corrections to $S1$ and $S2$ were made using the position dependence of the ^{131m}Xe deexcitation peak throughout the detector. The detector responses to high energy ER peaks, including 39.6 keV (n, ^{129}Xe*), 80.2 keV (n, ^{131}Xe*), 164 keV (^{131m}Xe), 236 keV (^{129m}Xe), 408 keV (^{127}Xe), 662 keV (^{137}Cs), and 1173 keV (^{60}Co), were used to determine the overall photon and electron detection efficiency. As in Ref. [3], the energy is reconstructed as

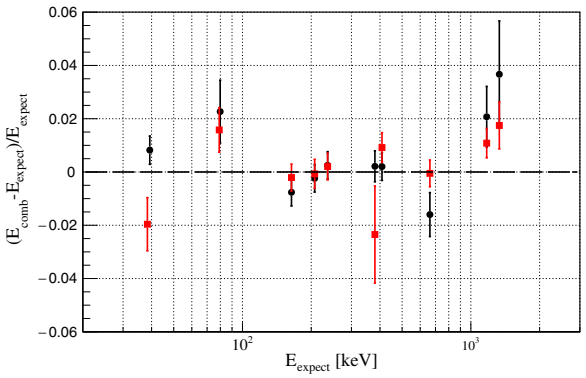

FIG. 1. Fractional difference between the reconstructed energy E_{comb} and the expected energy E_{expect} vs E_{expect} for ER peaks in Run 9 (black circles) and Run 10 (red squares), using the best fit PDE and EEE values described in the text. Uncertainties include both statistical and systematic components.

$$E_{\mathrm{comb}} = 0.0137\ \mathrm{keV}\left(\frac{S1}{\mathrm{PDE}} + \frac{S2}{\mathrm{EEE}\times\mathrm{SEG}}\right), \quad (1)$$

where PDE, EEE, and SEG are the photon detection efficiency, electron extraction efficiency, and single electron gain, respectively. The SEG was determined taking the charge distribution from the smallest $S2$ to be 24.4 ± 0.7 PE/e^- (Run 9) and 23.9 ± 0.5 PE/e^- (Run 10), with the ZLE efficiency taken into account. For an ER energy exceeding 200 keV, there were non-negligible saturation effects from the digitizers and the PMTs, for the $S2$ signal in particular. Like in the previous analysis, we used $S2_b$ ($S2$ from the bottom array) to reconstruct high energy events. However, in this analysis, $S2_b$ was corrected with a new $S2_b$ uniformity correction, different from the total $S2$ uniformity correction appropriate for the lower energy events. The saturation of $S2_b$ as a function of vertical position was also taken into account. In addition, instead of making cuts on $S1$ and $S2$ to select the ER peaks, we took all the data and performed a parameter scan in the PDE and EEE to fit E_{comb} peaks to the expected energies. The resulting best fit E_{comb} agreed with their expectation within 2% for the entire energy range considered (Fig. 1). The updated PDE and EEE were $11.14\% \pm 0.78\%$ and $54.5\% \pm 2.7\%$ for Run 9 and $11.34\% \pm 0.46\%$ and $57.7\% \pm 1.9\%$ for Run 10. Minor ZLE effects have been taken into account for the ER peaks in this analysis. Consistent values were obtained using low energy tritium events.

The neutron calibration data using an AmBe source (Ref. [3]) were reanalyzed with a significant improvement in the modeling. Some neutrons multiple scatter with a single energy deposition in the sensitive region and a partial energy deposition in the below-cathode region, where the electric field direction is opposite to the drift field in the target volume so the corresponding charge could not be detected. There are the so-called "neutron-X" events with an abnormally suppressed $S2/S1$ ratio, which mix with the

pure single scatter nuclear-recoil (NR) events. The vertical distribution in the calibration data was fitted with that expected from the GEANT4-based [14,15] MC simulation, from which the rates of the two components were separated statistically. Additional custom software then simulated the distribution of these events in $S1$ and $S2$. This simulation began with the detector field configuration, and then proceeded to the photon or electron productions and fluctuations based on the Noble Element Simulation Technique (NEST) framework [16]. It also incorporated the measured $S1$ and $S2$ spatial nonuniformity, channel-by-channel hit probability, double PE emissions [17] (probability measured to be 0.22 ± 0.02), ZLE effect, and the requirement on the number of fired PMTs be greater than three cut. A tuning on a single parameter $\alpha = N_{\rm ex}/N_i$, the ratio of the initial excitation to ionization, was performed in the NEST model, to match the 2D distribution in ($S1$, $S2$) between data and simulation for $S1 > 5$ PE and $S2_{\rm raw} > 200$ PE. The NR detection efficiency was then obtained by comparing the data and the simulation. In the "plateau region" for $S1 > 7$ PE and $S2_{\rm raw} > 200$ PE, the efficiency was anchored to 94%, derived from the number of events in the central part of the AmBe band before and after the data quality cuts. The tuned NR response model and its detection efficiency were used to produce the probability density functions (PDFs) for DM signals as well as the neutron background.

As described in Ref. [3], to characterize the detector response to the ER background, about 1×10^{-15} mol of CH_3T was loaded into the detector. The entire calibration run lasted for 44 days, but only the data in the first 18 hours were used in the previous paper, where the electron lifetime quickly deteriorated to an average 124 μs due to electronegative impurities. In this analysis, we chose a later data set with an average electron lifetime of 706 μs, which contained about 7500 low energy ER events in the fiducial volume (FV). The distribution of these events in $\log_{10}(S2/S1)$ vs $S1$ is shown in Fig. 2, with AmBe events overlaid. The NEST-based simulation mentioned above was then compared to the data. A tuning on α and a recombination fluctuation parameter for ER was performed, to match the median and width of the band for $S1 > 5$ PE. The ER detection efficiency was then extracted using the method mentioned earlier, and verified to be in agreement with that for NR. Below the reference NR median line, 40 events were identified, corresponding to a leakage of $0.53\% \pm 0.22_{\rm stat+sys}\%$, in good agreement with the MC prediction. The tuned NEST model was used to produce ER background PDFs.

There was significant background reduction in Run 10. The ^{127}Xe which was present in Run 9 had mostly decayed away. Some new ^{127}Xe background was introduced from a fresh surface xenon bottle, mixed in during the distillation. The average decay rate in Run 10 was estimated based on the 408 keV ER peaks to be 32 ± 6 μBq/kg. The corresponding 5 keV ER background in the DM search window is estimated

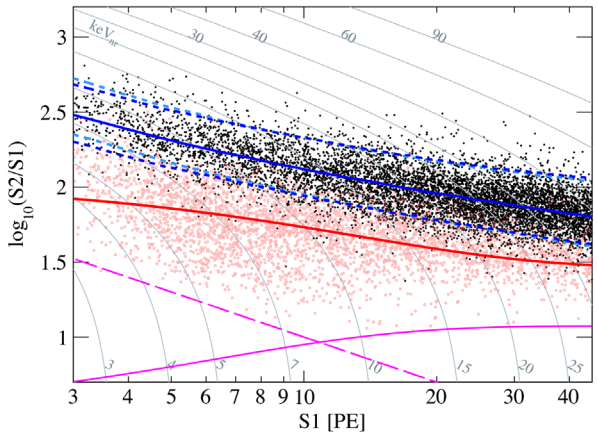

FIG. 2. Tritium (solid black dots) and AmBe data (open red circles) in $\log_{10}(S2/S1)$ vs $S1$. For comparison, the median (Runs 9 and 10 averaged, solid blue), 10% quantile, and 90% quantile (Run 9, dashed blue, Run 10, light dashed blue) of the ER background PDFs are overlaid. The solid red line is the median of the AmBe events. The dashed and solid magenta curves are the 100 PE selection cut for $S2$, and the 99.99% NR acceptance curve from the MC calculation, respectively. The gray curves represent the equal energy curves in nuclear recoil energy ($\rm keV_{nr}$).

to be 0.021 mDRU (1 mDRU $= 10^{-3}$ evt/kg/day/keV) with a 20% fractional uncertainty. The Kr background was measured in the data *in situ* using the delayed $\beta - \gamma$ coincidence. Thirteen events were found in the entire 580-kg sensitive volume. Taking the coincidence selection efficiency from the MC calculations, and assuming a 2×10^{-11} abundance of ^{85}Kr, the Kr concentration in Xe was 6.6 ± 2.2 ppt, more than a factor of 6 improvement from Run 9, contributing to an ER background of 0.20 ± 0.07 mDRU. From the energy spectrum of single-scatter events, a slight excess at low energy is consistent with a residual tritium background of 0.27 mDRU (left to float in the later likelihood fit). The Rn background, estimated based on the $\beta - \alpha$ coincidence of ^{214}Bi $-$ ^{214}Po and ^{212}Bi $-$ ^{212}Po, was 7.7 and 0.63 μBq/kg, respectively, consistent with the values measured in Run 9. The levels of the ER background are summarized in Table I.

The estimate of the accidental background has been improved in the present analysis. A random trigger run was set up to estimate the isolated $S1$ rate. The method in Run 9, searching for isolated $S1$-like signals before single $S1$ events (no $S2$), was found to be sometimes biased by real single scatter events whose $S2$ signals were misidentified as $S1$. Removing such effects reduced the isolated $S1$ rate by 14% to 1.6 Hz in Run 9. The isolated $S1$ rate in Run 10 was lowered to 0.4 Hz, possibly a direct consequence of the reduced PMT gain and dark rate mentioned earlier. The same boosted-decision-tree (BDT) cuts as in Run 9 (Ref. [3]) were used to suppress this background. The updated total (below-NR-median) accidental background is 12.2 (0.8) and 3.5 (0.5) for Run 9 and Run 10, respectively,

TABLE I. Summary of ER backgrounds from different components in Run 9 and Run 10. The tritium background for Run 10 in the table is based on the best fit to the data.

Item	Run 9 (mDRU)	Run 10 (mDRU)
^{85}Kr	1.19 ± 0.20	0.20 ± 0.07
^{127}Xe	0.42 ± 0.10	0.021 ± 0.005
^{3}H	0	0.27 ± 0.08
^{222}Rn	0.13 ± 0.07	0.12 ± 0.06
^{220}Rn	0.01 ± 0.01	0.02 ± 0.01
ER (material)	0.20 ± 0.10	0.20 ± 0.10
Solar ν	0.01	0.01
^{136}Xe	0.0022	0.0022
Total	1.96 ± 0.25	0.79 ± 0.16

with a 45% uncertainty estimated based on the variation of the isolated $S1$ rate in a given run period.

The neutron background, dominated by the radioactivity of the polytetrafluoroethylene (PTFE) materials, was estimated following the same approach as in Ref. [8], but with updated detector responses. The uncertainty is estimated to be 50% using the AmBe calibration data based on the ratio of detected single scatter NR events to the 4.4 MeV γ events.

The $S1$ and $S2$ range cuts were identical to those in Run 9, i.e., from 3 to 45 PE for $S1$, from 100 (raw) to 10 000 PE for $S2$, and above the 99.99% NR acceptance curve in Fig. 2. Remaining cuts were also kept the same as those in Run 9 except for the drift time cut. The lower cut was updated from 18 to 20 μs by scaling with the new drift speed (weaker field). The upper cut of 350 μs (310 μs in Run 9) was chosen since the rate of ^{127}Xe-induced "γ-X" events was reduced to be negligible. The same radius-square cut, $r^2 < 720$ cm^2, was used. The FV was computed geometrically, and the drift field uniformity was supported by the small position bias for events originating at the wall. Within the FV, the target mass was 361.5 ± 23.5 kg (328.9 kg in Run 9), where the uncertainty was estimated using tritium and radon events. The survival events after successive cuts are shown in Table II. The vertex distribution of events falling into the $S1$ and $S2$ windows is shown in Fig. 3. The distribution of events close to the PTFE wall with an abnormally small $S2$ and a nonuniform vertical distribution was attributed to the loss of electrons on the wall due to the local field irregularity. In Fig. 3(a), the red cluster close to $Z = 30$ cm is due to the peripheral top PMT with high noise and a high ZLE threshold [located in the upper right corner in Fig. 3(b)], causing a biased reconstructed position particularly for wall events with suppressed $S2$ deep in the TPC. In the FV, the residual events are uniformly distributed. In total, there are 177 final candidate events. The distribution of $\log_{10}(S2/S1)$ vs $S1$ of these events is shown in Fig. 4, mostly consistent with the ER background. For reference, no events are identified below the NR median line, with a 1.8 ± 0.5 expected background, indicating a downward fluctuation of the background. In combination with the below-NR events in Run 9 (Table III), the probability of observing one or less events when five are expected is 7.2%.

TABLE II. Number of events in Run 9 and Run 10 after successive analysis selections.

Cut	Run 9	Run 10
All triggers	24 502 402	18 369 083
Quality cuts	5 160 513	3 070 111
$S1$ and $S2$ range	131 097	111 854
FV cut	398	178
BDT cut	389	177

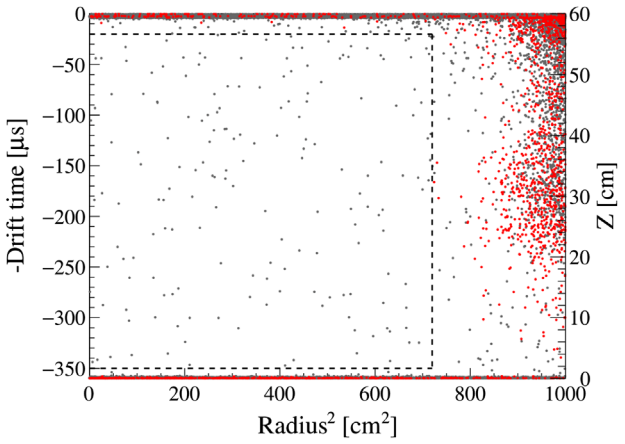

(a) The r^2-z distribution.

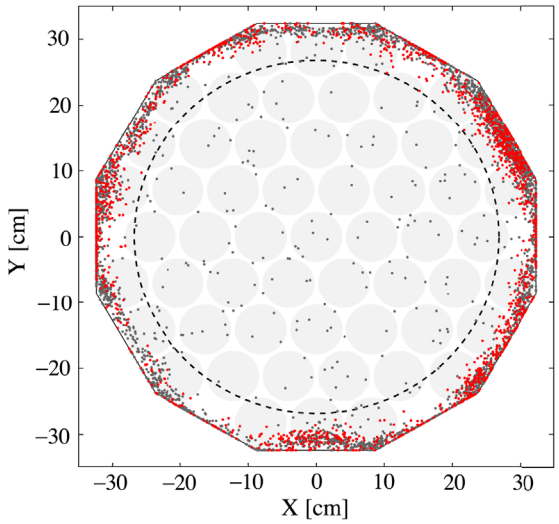

(b) The x-y distribution.

FIG. 3. The position distributions for events within the $S1$ and $S2$ range cuts. (a) z vs r^2 and (b) y vs x. The drift time cut between 20 and 350 μs is applied for (b). The gray and red points are events above and below the NR median, respectively. The dashed box (a) and circle (b) represent the FV cut. The gray background circles in (b) indicate locations of the top PMTs.

TABLE III. The best fit total and below-NR-median background events in Run 9 and Run 10 in the FV. The fractional uncertainties of expected events in the table are 13% (Run 9 ER), 20% (Run 10 ER), 45% (accidental), and 50% (neutron), respectively, and are propagated into that for the total fitted events. The below-NR-median ER background for Run 9 was updated using the new ER calibration. The corresponding best fit background nuisance parameters [δ_b's in Eq. (2)] are 0.123 (^{127}Xe), 0.135 (tritium), −0.105 (flat ER), 0.111 (accidental), and −0.098 (neutron). The number of events from the data are shown in the last column.

	ER	Accidental	Neutron	Total Fitted	Total Observed
Run 9	376.1	13.5	0.85	390 ± 50	389
Below NR median	2.0	0.9	0.35	3.2 ± 0.9	1
Run 10	172.2	3.9	0.83	177 ± 33	177
Below NR median	0.9	0.6	0.33	1.8 ± 0.5	0

The final candidates in Runs 9 and 10 were combined to search for WIMPs. An unbinned likelihood function was constructed as

$$\mathcal{L}_{\text{pandax}} = \left[\prod_{n=1}^{\text{nset}} \mathcal{L}_n\right] \times \left[G(\delta_{\text{DM}}, \sigma_{\text{DM}}) \prod_b G(\delta_b, \sigma_b)\right], \quad (2)$$

where

$$\mathcal{L}_n = \text{Poiss}(N^n_{\text{meas}} | N^n_{\text{fit}}) \times \left[\prod_{i=1}^{N^n_{\text{meas}}} \left(\frac{N^n_{\text{DM}}(1+\delta_{\text{DM}}) P^n_{\text{DM}}(S1^i, S2^i)}{N^n_{\text{fit}}} + \sum_b \frac{N^n_b(1+\delta_b) P^n_b(S1^i, S2^i)}{N^n_{\text{fit}}}\right)\right]. \quad (3)$$

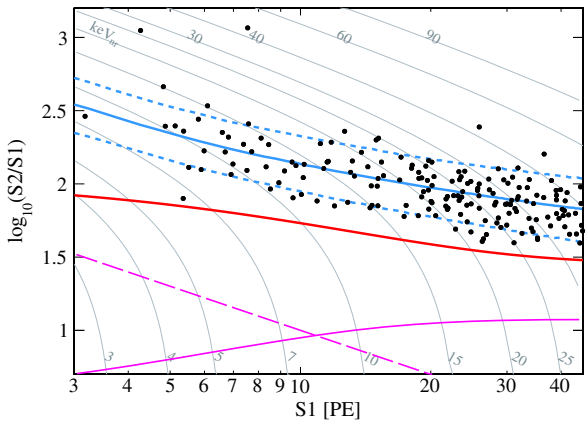

FIG. 4. The distribution of $\log_{10}(S2/S1)$ vs $S1$ for the DM search data in Run 10, overlaid with the corresponding median, 10% quantile, and 90% quantile of the ER background PDFs. The red curve is the NR median from the AmBe calibration.

As in Ref. [3], the data were divided into 14 sets in Run 9, and four sets in Run 10 (nset = 18) to reflect different operation conditions in the TPC fields and electron lifetime. For each data set n, N^n_{meas} and N^n_{fit} represent the measured and fitted total numbers of detected events; N^n_{DM} and N^n_b are the numbers of WIMP and background events, with their corresponding PDFs $P^n_{\text{DM}}(S1, S2)$ and $P^n_b(S1, S2)$. The detection efficiencies needed for determining the detected numbers of events are either contained in the PDF, or

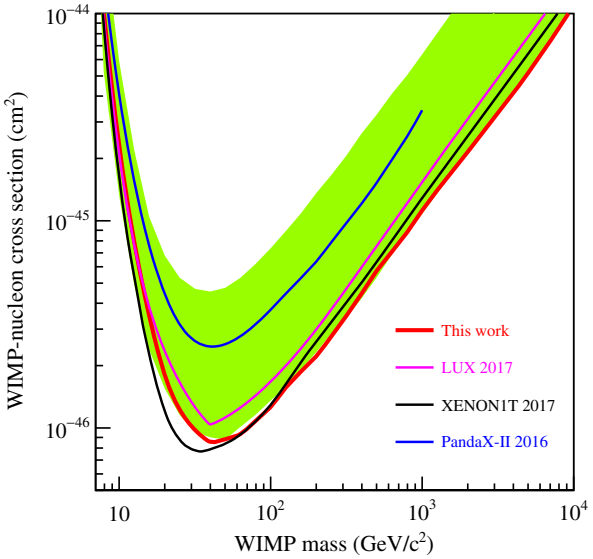

(a) log scale in m_x

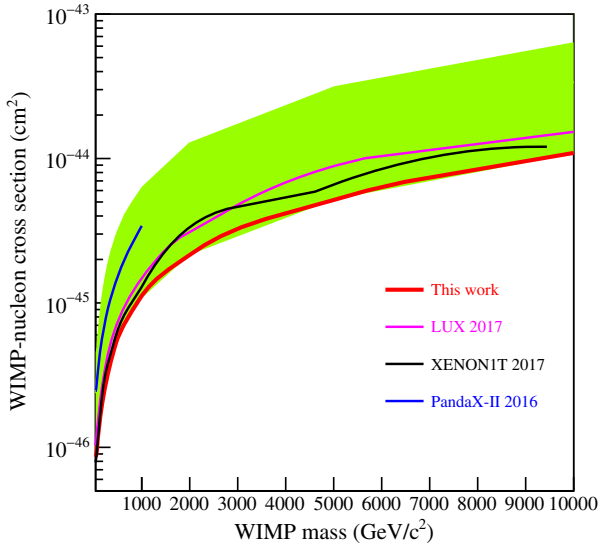

(b) linear scale in m_x

FIG. 5. The 90% C.L. upper limits versus m_χ [(a) log scale, (b) linear scale between 40 GeV/c^2 and 10 TeV/c^2] for the spin independent WIMP-nucleon elastic cross sections from the combined PandaX-II Run 9 and Run 10 data (red), overlaid with that from PandaX-II 2016 [3] (blue), LUX 2017 [2] (magenta), and XENON1T 2017 [4] (black). The green band represents the $\pm 1\sigma$ sensitivity band.

included in N_b (accidental background). Five background components (represented by the subscript "b") are considered, including ^{127}Xe, tritium, other flat ER (^{85}Kr, radon, and other detector gamma background), accidental, and neutron background. Among all data sets, δ_b and σ_b are the common nuisance normalization parameters and fractional systematic uncertainties, respectively, with σ_b taken from Table I, and $G(\delta_b, \sigma_b)$ is the Gaussian penalty term. For WIMP detection, we also assumed a normalization nuisance parameter $\delta_{\rm DM}$ constrained by a $\sigma_{\rm DM}$ of 20%, conservatively estimated using different NR models as well as the uncertainties in PDE and EEE. The ER and NR background PDFs were generated using the tuned NEST models, and the accidental PDFs were produced from randomly paired data. The WIMP spectrum was calculated using the same formalism as in Refs. [18,19], including all the nuclear and astronomical input parameters (standard isothermal halo model with a DM density of 0.3 GeV$/c^2/$cm^3). The WIMP PDFs at different masses m_χ were produced using the tuned NR model with the detection efficiency embedded. For all WIMP masses between 5 GeV$/c^2$ and 10 TeV$/c^2$, the best fit cross section was always zero, and the best fit nuisance parameters were all within 1σ of the nominal values. The standard profile likelihood test statistic was used to set the exclusion limit on the spin independent WIMP-nucleon elastic scattering cross section $\sigma_{\chi,n}$ [20,21]. The test statistic was calculated at grids of (m_χ, $\sigma_{\chi,n}$) for the data, and compared to those obtained from a large number of toy Monte Carlo calculations produced and fitted using the same signal hypotheses [22]. The final 90% C.L. limit is shown in Fig. 5, together with limits from PandaX-II 2016 [3], LUX [2], and XENON1T [4] (see also Fig. 18 in the Supplemental Material [11]). The limit is very close to the -1σ of the sensitivity band for a WIMP mass above 20 GeV$/c^2$; therefore, power constraining [23] the limit to -1σ of the sensitivity would make little difference. The strongest limit is set to be 8.6×10^{-47} cm^2 at the WIMP mass of 40 GeV$/c^2$. The limit curve corresponds to on average 2.3 signal events across the full mass range, e.g., 1.9 at 10 GeV$/c^2$ and 2.6 at 1 TeV$/c^2$. This limit is about a factor of 3 more constraining than our previous results [3] (using the so-called CL$_s$ approach [24,25]), and represents the most stringent limit on the elastic WIMP-nucleon spin-independent cross section for a WIMP mass larger than 100 GeV$/c^2$.

In summary, we report the combined WIMP search results using the data with an exposure of 54 ton days, the largest of its kind, from the PandaX-II experiment. Like the previous attempts, no WIMP candidates have been identified. This yields a most stringent limit for the WIMP-nucleon cross section for masses larger than 100 GeV$/c^2$. Theoretical models indicate the importance of enhancing the current search sensitivity by another order of magnitude. The PandaX-II detector will continue to run until a future upgrade to a multiton scale experiment at CJPL.

This project has been supported by a 985-III grant from Shanghai Jiao Tong University, grants from the National Natural Science Foundation of China (Grants No. 11365022, No. 11435008, No. 11455001, No. 11505112, and No. 11525522), and a grant from the Ministry of Science and Technology of China (Grant No. 2016YFA0400301). We acknowledge the support of grants from the Office of Science and Technology, Shanghai Municipal Government (Grants No. 11DZ2260700, No. 16DZ2260200), and the support from the Key Laboratory for Particle Physics, Astrophysics and Cosmology, Ministry of Education. This work is supported in part by the Chinese Academy of Sciences Center for Excellence in Particle Physics (CCEPP) and the Hongwen Foundation in Hong Kong. We also would like to thank Dr. Xunhua Yuan and Chunfa Yao of the China Iron and Steel Research Institute Group, and the Taiyuan Iron and Steel (Group) Co. Ltd. for crucial help on low background stainless steel. Finally, we thank the following organizations for indispensable logistics and other supports: the CJPL administration and the Yalong River Hydropower Development Company Ltd.

*Corresponding author.
jianglai.liu@sjtu.edu.cn
†Corresponding author.
anditan@umd.edu
‡Corresponding author.
wangqiuhong@sinap.ac.cn
§Spokesperson.
xdji@sjtu.edu.cn

[1] G. Bertone, D. Hooper, and J. Silk, Phys. Rep. **405**, 279 (2005).
[2] D. S. Akerib *et al.* (LUX Collaboration), Phys. Rev. Lett. **118**, 021303 (2017).
[3] A. Tan *et al.* (PandaX-II Collaboration), Phys. Rev. Lett. **117**, 121303 (2016).
[4] E. Aprile *et al.* (XENON Collaboration), following Letter Phys. Rev. Lett. **119**, 181301 (2017).
[5] E. A. Bagnaschi *et al.*, Eur. Phys. J. C **75**, 500 (2015).
[6] J. Liu, X. Chen, and X. Ji, Nat. Phys. **13**, 212 (2017).
[7] K. J. Kang, J. P. Cheng, Y. H. Chen, Y. J. Li, M. B. Shen, S. Y. Wu, and Q. Yue, J. Phys. Conf. Ser. **203**, 012028 (2010).
[8] A. Tan *et al.* (PandaX Collaboration), Phys. Rev. D **93**, 122009 (2016).
[9] D. S. Akerib *et al.* (LUX Collaboration), Phys. Rev. D **93**, 072009 (2016).
[10] http://www.caen.it/servlet/checkCaenManualFile?Id=12364.
[11] See Supplemental Material at http://link.aps.org/supplemental/10.1103/PhysRevLett.119.181302, for [brief description], which includes Refs. [2,3,4,12].

[12] X. Ji, in *TeV Particle Astrophysics 2017* (Columbus, Ohio, US, 2017); https://tevpa2017.osu.edu/talks/ji.pdf.
[13] Q. Wu *et al.*, J. Instrum. **12**, T08004 (2017).
[14] S. Agostinelli *et al.* (GEANT4), Nucl. Instrum. Methods Phys. Res., Sect. A **506**, 250 (2003).
[15] J. Allison *et al.*, IEEE Trans. Nucl. Sci. **53**, 270 (2006).
[16] B. Lenardo, K. Kazkaz, M. Szydagis, and M. Tripathi, IEEE Trans. Nucl. Sci. **62**, 3387 (2015).
[17] C. H. Faham, V. M. Gehman, A. Currie, A. Dobi, P. Sorensen, and R. J. Gaitskell, J. Instrum. **10**, P09010 (2015).
[18] M. Xiao *et al.* (PandaX Collaboration), Sci. China Phys. Mech. Astron. **57**, 2024 (2014).
[19] X. Xiao *et al.* (PandaX Collaboration), Phys. Rev. D **92**, 052004 (2015).
[20] G. Cowan, K. Cranmer, E. Gross, and O. Vitells, Eur. Phys. J. C **71**, 1554 (2011); **73**, 2501(E) (2013).
[21] E. Aprile *et al.* (XENON100 Collaboration), Phys. Rev. D **84**, 052003 (2011).
[22] G. J. Feldman and R. D. Cousins, Phys. Rev. D **57**, 3873 (1998).
[23] G. Cowan, K. Cranmer, E. Gross, and O. Vitells, arXiv: 1105.3166.
[24] A. L. Read, J. Phys. G **28**, 2693 (2002).
[25] T. Junk, Nucl. Instrum. Methods Phys. Res., Sect. A **434**, 435 (1999).